The Narrow-Band Assumption in Log-Chromaticity Space

Eva Eibenberger[1,2,3] and Elli Angelopoulou[1,3]

[1]Pattern Recognition Lab, University of Erlangen-Nuremberg, Germany
[2]International Max Planck Research School for Optics and Imaging
[3]Erlangen Graduate School in Advanced Optical Technologies (SAOT), Erlangen, Germany
{eva.eibenberger,elli.angelopoulou}@informatik.uni-erlangen.de

Abstract. Despite the strengths and popularity of the log-chromaticity space (LCS), there is still a significant amount of concern regarding its narrow-band assumption (NBA). Though not always necessary, this assumption is relatively common, as it leads to elegant formulations. We present a scheme for evaluating whether a deviation from the NBA will have an impact on the expected LCS values. We also introduce two metrics for measuring the divergence from the expected behavior under the NBA in LCS. Lastly, we empirically analyze how different types of reflectance spectra are affected in varying degrees by this assumption. For example, experiments with real and synthetic data show that the violation of the NBA typically has insignificant impact on bright unsaturated colors.

1 Introduction

Many applications in computer vision, like tracking, image retrieval, and object recognition are affected by variations in the illumination conditions. Therefore, a considerable amount of research has been focused on the development of illumination-invariant color spaces [1, 2]. One such color space is the log-chromaticity space (LCS). The transformation of RGB values (I_R, I_G, I_B) to this space is done by first computing the 2D chromaticity values $\{I_R/I_G, I_B/I_G\}$ and then taking the logarithm of these color ratios. Two important properties are provided by this transformation: Firstly, a surface color seen under different illuminant colors tends to lie on a straight line in this space. Secondly, for a given camera, all these lines are parallel to each other for different surface colors. These two characteristics of LCS make it a very promising space for color and reflectance analysis. Hence, LCS is already quite widely used for applications like shadow removal [3–7], illumination estimation [8] and illumination invariant representations [1].

Many of these techniques make an additional assumption, the so-called *narrow-band assumption* (NBA) (e.g. [9, 4–7]), which states that the sensor spectral sensitivities can be approximated by delta Dirac functions. Though this assumption leads to elegant and tractable mathematical formulations, most available sensors

exhibit non-narrow spectral sensitivities. Therefore, it is often argued that this assumption is too restrictive and not generally applicable [10–12].

In order to broaden the applicability of methodologies that assume narrow-spectral bands, *sensor sharpening* algorithms have been proposed [13–15]. Although, sensor sharpening enhances color constancy performance [16], its biggest limitation is the required camera calibration, which is can be tedious [16, 5]. Furthermore, sharpening can only be performed if the sensor is available. Thus, it can not be applied on arbitrary images (like those found on the web), where the sensor is not available for calibration.

In this paper we evaluate the error in LCS values that is introduced by the violation of the NBA. We show that although deviations from the expected behavior in LCS can occur, it is often the case that for certain families of reflectivity (albedo) the violation of the Dirac delta assumption does not affect the LCS values. Due to the image formation process, it is difficult to separate the influences of the sensor characteristics, the illumination and the surface reflectance. In our efforts to address this challenge, we were influenced by previous evidence that for certain materials, like asphalt and skin, the violation of the NBA has minimal impact [11, 17]. Therefore, we chose to focus our analysis on the suitability of the NBA for different surface reflectances. We introduce a new formulation which explicitly describes the deviation from the NBA. We then propose two error metrics for quantitative evaluation of the impact of the deviation. Our experiments on both synthetic and real data show that these error metrics can be used for determining whether a particular material is unaffected by possible violations of the NBA. Such an assessment can have a direct impact on broadening the applicability of LCS methods on arbitrary images.

2 Theory of the Log-Chromaticity Space

In order to systematically assess the impact of the NBA in the LCS one needs to first closely examine the image formation process as well as the influence of the incident illumination.

2.1 Planckian Illuminant

Empirical measurements of daylight spectra [18] have shown that outdoor light as well as indoor illuminants (CIE standard illuminants between $4000K$ and $13000K$) closely fit the corresponding black body radiators. The behavior of a black body radiator is in turn described by Planck's law. For the visible range $\exp(\frac{c_2}{\lambda T}) \gg 0$ and thus one can use Wien's approximation for describing the spectral distribution $E(\lambda, T)$ of such illuminants:

$$E(\lambda, T) \approx I c_1 \lambda^{-5} \exp\left(-\frac{c_2}{T\lambda}\right), \tag{1}$$

where λ and T are the wavelength and illuminant temperature respectively, $c_1 = 2\pi h v^2$ and $c_2 = hv/k$ are constants containing the Planck constant h, the

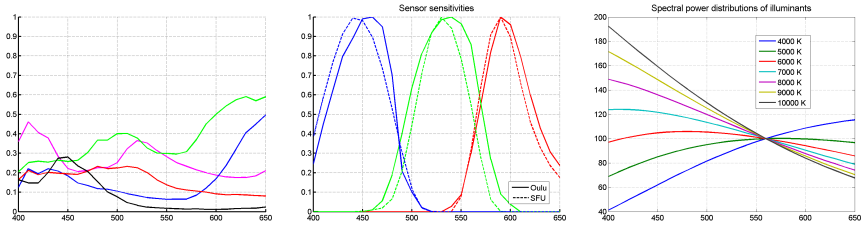

(a) (b) (c)

Fig. 1. Image formation. (a) Surface reflectance functions. (b) Sensor sensitivities. (c) Spectral power distributions of Planckian illuminants.

Boltzmann constant k, and the speed of light v in vacuum. As in Finlayson and Hordley [9], the intensity constant I is introduced to model the varying intensity power. Fig. 1(c) shows the emission spectra of different color temperatures.

2.2 Image Formation

An image captured by a typical color camera can be modeled as:

$$I_c(\mathbf{x}) = g\left(\int_\Omega q_c(\lambda)S(\mathbf{x},\lambda)E(\mathbf{x},\lambda)d\lambda\right)^{\frac{1}{\gamma}}, \quad c \in \{R,G,B\}\,. \tag{2}$$

This equation states that at a position $\mathbf{x}$ the sensor response for a certain color channel c is a combination of the sensor sensitivity q_c, the illumination E and the surface reflectance S. The integral is computed over the visible spectrum Ω. In order to incorporate further sensor characteristics we also consider the camera gain g and gamma γ. The image sharpening, which is also often built-in in modern digital cameras, is not considered in this context, as the proposed analysis is not based on spatial but rather only on color information. Fig. 1 shows the three components of image formation.

The *narrow-band assumption* (NBA) [9, 6] directly affects the image formation model. This assumption states that the sensor sensitivities are considered to be Dirac delta functions, $q_c(\lambda) = k_c\delta(\lambda - \lambda_c)$, centered at wavelength λ_c. Assuming a constant illuminant color across the scene, Eq. 2 becomes:

$$I_c(\mathbf{x}) = g k_c^{\frac{1}{\gamma}} S(\mathbf{x},\lambda_c)^{\frac{1}{\gamma}} E(\lambda_c)^{\frac{1}{\gamma}}. \tag{3}$$

2.3 The Log-Chromaticity Color Space

Among the different chromaticity spaces, we choose to use the ratios of the red and blue channel with respect to green (as in [9]). By combining Eq. 1 and Eq. 3 the chromaticity values become

$$\frac{I_c(\mathbf{x})}{I_G(\mathbf{x})} = \frac{k_c^{\frac{1}{\gamma}} S(\mathbf{x},\lambda_c)^{\frac{1}{\gamma}} \left(\lambda_c^{-5}\exp\left(-\frac{c_2}{T\lambda_c}\right)\right)^{\frac{1}{\gamma}}}{k_G^{\frac{1}{\gamma}} S(\mathbf{x},\lambda_G)^{\frac{1}{\gamma}} \left(\lambda_G^{-5}\exp\left(-\frac{c_2}{T\lambda_G}\right)\right)^{\frac{1}{\gamma}}} \quad c \in \{R,B\}\,. \tag{4}$$

In order to remove the γ-nonlinearity and the exponential function in Wien's approximation, we take the natural logarithm. Furthermore, we model the surface reflectance as diffuse reflectance $S(\mathbf{x}, \lambda) = w_d(\mathbf{x})\rho(\mathbf{x}, \lambda)$, which can be decomposed to a wavelength-independent geometric factor $w_d(\mathbf{x})$ and a material dependent albedo $\rho(\mathbf{x}, \lambda)$ at a certain position $\mathbf{x}$. Thus, the LCS value of a diffuse surface at a particular point $\mathbf{x}$ is:

$$r_{c,G} = \ln(\frac{I_c}{I_G}) = \frac{1}{\gamma}\ln(\frac{\rho_c}{\rho_G}) + \frac{1}{\gamma}\ln(k_c k_G^{-1}\lambda_c^{-5}\lambda_G^5) + \frac{1}{\gamma}\frac{1}{T}(\frac{c_2}{\lambda_G} - \frac{c_2}{\lambda_c}) \ . \quad (5)$$

$r_{R,G}$ and $r_{B,G}$ are then the LCS values of a particular pixel $\mathbf{x}$. This color space is also known as the log-ratio space and log-chromaticity differences [9]. Please note that for the remainder of the paper we omit writing that the log-chromaticity $\mathbf{r}$, the image value I, the geometry term w_d and the albedo ρ are functions on $\mathbf{x}$.

If we consider the LCS values of a pixel to be a point in the 2D vector space, the point coordinates are given by

$$\mathbf{r} = \begin{pmatrix} r_{R,G} \\ r_{B,G} \end{pmatrix} = \frac{1}{\gamma}\underbrace{\begin{pmatrix} \ln(\frac{\rho_R}{\rho_G}) \\ \ln(\frac{\rho_B}{\rho_G}) \end{pmatrix}}_{\mathbf{s}_\rho} + \frac{1}{\gamma}\underbrace{\begin{pmatrix} \ln(k_R k_G^{-1}\lambda_R^{-5}\lambda_G^5) \\ \ln(k_B k_G^{-1}\lambda_B^{-5}\lambda_G^5) \end{pmatrix}}_{\mathbf{b}} + \frac{1}{\gamma}\frac{1}{T}\underbrace{\begin{pmatrix} \frac{c_2}{\lambda_G} - \frac{c_2}{\lambda_R} \\ \frac{c_2}{\lambda_G} - \frac{c_2}{\lambda_B} \end{pmatrix}}_{\mathbf{d}} \ . \quad (6)$$

This equation illustrates that in the LCS all the color values of an albedo seen under different illuminants fall on a straight line. The line is defined by a point lying on $(\frac{1}{\gamma}\mathbf{s}_\rho + \frac{1}{\gamma}\mathbf{b})$ and the direction $\mathbf{d}$. The position of the line is dependent on the albedo ρ and the sensor characteristics (k_R, k_G, k_B, λ_R, λ_G and λ_B) The scaling factor $\frac{1}{T}$ denotes that depending on the illumination color (defined by the temperature T) the same material color ρ will fall on a different position of the same line. Note that the slope of the line $\mathbf{d}$ is independent of the material. As a consequence, different albedos will lie on different lines, as vector $\mathbf{s}_\rho$ changes. However, all these lines are parallel, since they share the same slope. The factor $1/\gamma$ only causes a constant scaling of the vectors. Thus, the LCS exhibits two key characteristics (see dotted lines in Fig. 2(b)): Firstly, **linearity** (As the illuminant color changes the LCS values of a surface fall on a straight line, pointing in the so-called invariant direction [1]) and secondly, **parallelism** (For a given camera, all such lines for different surface colors are parallel). Both properties are extremely helpful for illumination invariance, as a normalized image can be generated although the illuminant color is unknown or inhomogeneous across the image (like shadow regions). On the other hand, the violation of the NBA may disarrange the linearity and parallelism in LCS (see crosses in Fig. 2(b)).

3 Influence of the Narrow-Band Assumption

In order to analyze the influence of the NBA, we have to establish a scheme for estimating the introduced error. The sensor sensitivities can be better approximated by Gaussian functions with means $\mu = \lambda_c$ and standard deviation σ (see Fig. 1(b)). The standard deviation can be seen as the descriptor for the

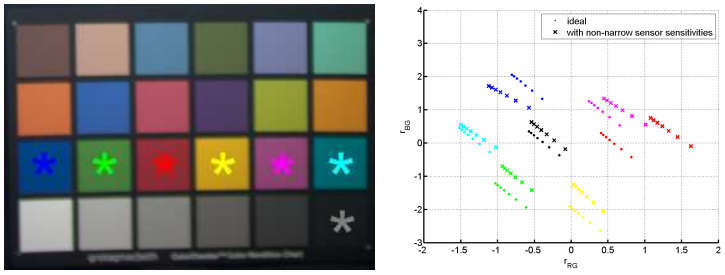

(a) (b)

Fig. 2. (a) Sample reflectances. (b) LCS values of the different color patches. The ideal values form parallel straight lines.

narrowness of the sensitivities. Assuming for clarity of presentation $g = 1$, $\gamma = 1$, $k_c = 1$, Eq. 2 is then transformed to:

$$I_c(\mathbf{x}) = w_d(x) I c_1 \frac{1}{\sqrt{2\pi}\sigma} \int_\Omega \rho(\mathbf{x}, \lambda) \mathrm{e}^{-\frac{c_2}{T\lambda}} \mathrm{e}^{-\frac{(\lambda-\lambda_c)^2}{2\sigma^2}} d\lambda, \tag{7}$$

In this formula we assume diffuse reflectance and a Planckian illuminant $E(\lambda, T)$ as in Eq. 1. As this equation shows, there are three factors influencing the deviation from the Dirac delta assumption: the albedo $\rho(\lambda)$ of the material, the standard deviation of the sensor sensitivities, and the color temperature T of the illuminant. Since, for arbitrary images the illuminant is typically unknown, we focus our error analysis on the influence of the albedo $\rho(\lambda)$ and the filter width σ. Such an analysis will then allow one to either safely use the Dirac assumption or avoid it depending on the scene materials.

By rearranging Eq. 7, we obtain:

$$I_c = w_d I c_1 \left(\underbrace{\rho(\lambda_c) \mathrm{e}^{-\frac{c_2}{T\lambda_c}}}_{D_c} + \underbrace{\int_{\Omega \setminus \lambda_c} \rho(\lambda) \mathrm{e}^{-\frac{c_2}{T\lambda}} \frac{1}{\sqrt{2\pi}\sigma} \mathrm{e}^{-\frac{(\lambda-\lambda_c)^2}{2\sigma^2}} d\lambda}_{Q_c} \right), \tag{8}$$

Thus, the LCS values can then be expressed as:

$$r_{c,G} = \ln\left(\frac{I_c}{I_G}\right) = \ln\left(\frac{Q_c + D_c}{Q_G + D_G}\right), \tag{9}$$

where D_c corresponds to the ideal intensity assuming Dirac delta functions and Q_c corresponds to the error which is introduced when employing cameras with wider sensor sensitivities. Hence, in order to have an error as minimal as possible, the ratio inside the logarithm of Eq. 9 has to be as close as possible to the ideal ratio D_c/D_G. This is equivalent to requiring that

$$Q_B D_R = Q_R D_B \quad \text{or} \quad \frac{Q_B}{Q_R} = \frac{D_B}{D_R}, \tag{10}$$

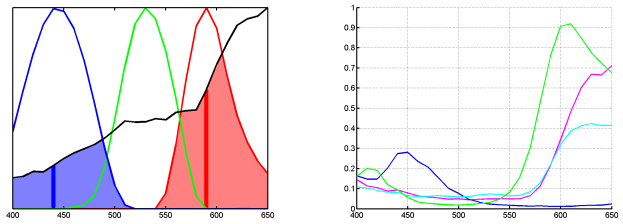

(a) (b)

Fig. 3. Impact of the NBA. (a) The red and blue vertical lines are the sensor responses under the Dirac delta assumption. The shaded regions denote the error due to non-narrow sensor sensitivities. There is no impact on the LCS values if the ratio of the shaded regions is equal to the ratio of the corresponding vertical lines. (b) The diversity of the shape of the spectra makes the error analysis difficult.

which is obtained when $(Q_R+D_R)/(Q_G+D_G) = D_R/D_G$ and $(Q_B+D_B)/(Q_G+D_G) = D_B/D_G$. This means that the ratio of the errors in the red and blue channel has to be equal to the ratio of the Dirac responses. Fig. 3(a) illustrates this relation. This means that as long as the ratio in Eq. 10 is satisfied, one can use the NBA, even though $Q_c \neq 0$. On the other hand, if the combination of a sensor sensitivity with the spectrum of an albedo causes an inequality in this relation, the position of the resulting values and the ideal Dirac values will differ in LCS. It is important to note that this relation is dependent on the temperature of the illuminant. Furthermore, the diversity of the shape of real spectra makes this analysis difficult.

4 Experiments

Our goal is to systematically evaluate the impact of the deviation from the NBA on the LCS. Unfortunately, the non-separability of the different factors of image formation make the analytic estimation of Eq. 9 and Eq. 10 intractable for arbitrary images. We can however measure for specific surface spectra $\rho(\lambda)$ and for different filter widths σ how deviations from the NBA affect the position and orientation of the invariant lines in LCS.

We computed the product of different albedo curves with Planckian illuminants and different sensor sensitivities. The resulting RGB values were transformed in LCS and the resulting deviations were evaluated using three different error measures. We analyzed spectra of both synthetic and real data. We simulated different spectral sensitivities by using Gaussians of varying σ.

4.1 Data

For the evaluation of synthetic reflectance curves, 36 lines of different slopes and intensity levels have been generated (see Fig. 6). For analysis of real reflectances, we used about 160 different reflectance spectra which were extracted

from the CAVE database [19]. In order to gain insight into the influence of their shape on the introduced error, the spectra have been categorized into 37 groups according to their shape. Examples for shape-categories are shown in Fig. 5. Furthermore, 357 skin reflectance curves (from 119 different persons) of the UOPB Face Database [20] have been analyzed in Sec. 4.6.

As examples of sensor sensitivities we took the spectral responses from two 3CCD cameras: a Sony DXC-755P [20] (denoted as "Oulu" in our plots) and a Sony DXC-930 [21] (denoted as "SFU"), see Fig. 1(b). There is a mismatch of the wavelength-range between the natural reflectance curves from the CAVE database ($\lambda \in [400\,nm, 700\,nm]$) and the sensor sensitivities. The sensors have a non-zero sensitivity at $\lambda < 400\,nm$, while the sensitivity at $\lambda > 700\,nm$ is zero. In order to avoid asymmetry in the resulting log-chromaticities due to this spectral cut off, we limited the spectral range to $\lambda \in [400\,nm, 650\,nm]$. For the evaluation we selected $T \in [4000\,K, 10000\,K]$ and the dominant wavelength of the dirac Delta functions as $\lambda_G = 450$, $\lambda_B = 530$ and $\lambda_R = 590$ with $k_B = k_G = k_R = 1$.

4.2 Error Measures

The error analysis is performed on the basis of three error measures: the *angular error* ϵ_{ang}, the *average distance* ϵ_{dist} and the *difference of ratios* ϵ_{rat}. The *angular error* $\epsilon_{ang} \in [0°, 90°]$ defines the angle between the invariant line l_{Dirac} obtained with the Dirac functions and the invariant line l_{sens} computed using non-Dirac sensor sensitivities. Not only the parallelism of the two lines is affected, but also a shift between line l_{sens} and l_{Dirac} can be observed. Thus, we define a second error metric, the *average distance* ϵ_{dist} between the LCS values of the sensor sensitivities r_{cG} and those of the Dirac function $\hat{r}_{cG}$ as:

$$\epsilon_{dist} = \sum_{T=4000}^{10000} \sqrt{(r_{RG}(T) - \hat{r}_{RG}(T))^2 + (r_{BG}(T) - \hat{r}_{BG}(T))^2}, \qquad (11)$$

Depending on the application ϵ_{dist} (clustering/segmentation in LCS) or ϵ_{ang} (illumination-invariant representation) is more important.

We also evaluated the deviation from Eq. 10 by computing the difference between the two ratios. We denote this error measure as *difference of ratios* ϵ_{rat} and compute it as:

$$\epsilon_{rat}(T) = (Q_B(T)/Q_R(T)) - (D_B(T)/D_R(T))\,. \qquad (12)$$

Note that both ϵ_{dist} and ϵ_{rat} are explicitly dependent on the temperature of the illuminant. In our analysis it turned out that the correlation of ϵ_{rat} and ϵ_{ang} was extremely high. In order to avoid redundancy we limited parts of our presentation to ϵ_{ang}.

4.3 Synthetic Surface Reflectances

In order to analyze the influence of a) the reflectance level and b) the general shape of the albedo on the accuracy of the LCS values, we generated linear

reflectance spectra with different slopes and intercepts (see Fig. 6). Several important observations can be made:

1. The **slope** of the line: The slope of the line influences the average error ϵ_{dist}. The larger the slope of the line, the smaller ϵ_{dist} (see e.g. Fig. 6(i), 6(l)). In all the analyzed curves, ascending lines lead to a smaller ϵ_{dist} than descending lines (see Fig. 6(c), 6(f), 6(i), 6(l)). This observation can be explained by the shape of the sensor sensitivities. Consider a horizontal albedo. As the blue filter is often broader than the red one, the error in blue will be larger than in red ($Q_B > Q_R$) while for the ideal values they will be equal ($D_B = D_R$). In order to achieve a more balanced ratio of Eq. 10, the albedo needs to have a smaller level in the blue part of the spectrum.
2. The **level** of the reflectance curves: In most analyzed curves it was observable that the angular error ϵ_{ang} decreases with increasing level of intensity (see e.g. Fig. 6(c), 6(i), 6(l)). Again, let us consider two horizontal albedos of different reflectivity levels. As the blue filter is wider, the error in the blue channel is larger than in the red one. However, closer to the dominant wavelength, the difference between the red and blue curves is decreasing. Therefore, the higher the intensity level, the smaller the additional error in the blue channel and the better the error ratio.

Furthermore, it seems that the average distance ϵ_{dist} is affected more by variations in the shape of the albedo curves, while the angular error ϵ_{ang} is more sensitive to the overall level of reflectivity.

4.4 Real Surface Reflectances

Similar trends can also be observed for real reflectance data. However, due to the more complex structure of the albedo curves and the simultaneous variation in shape and level, the interpretation of the results is less intuitive than for the synthetic data.

1. **Balancing** of the red and blue part of the albedo: Similar to the synthetic data, Fig. 5(c) illustrates that albedos with slightly increasing slopes result in a low ϵ_{dist}, as the ratio of Eq. 10 is well balanced. This observation is also supported by the example in Fig. 5(f). If the error in the blue band is too high compared to the error in the red one (see Fig. 7(f)) or the other way around (see Fig. 7(c)) both errors, ϵ_{dist} and ϵ_{ang}, increase.
2. The **level** of the reflectance curves: Here again, it can be nicely observed that an increased reflectivity reduces the angular error ϵ_{ang}. This effect is illustrated in Fig. 5(i).
3. **Minimal level** of reflectivity: Closely related to the previous investigation is the observation that extremely small levels (e.g. $\rho(\lambda) < 0.03$) over some parts of the considered wavelengths result in an increased error. For instance, this is observable is Fig. 7(i), where the curve with the highest level in the range of $\lambda \in [400\,nm, 570\,nm]$ results in the lowest error.

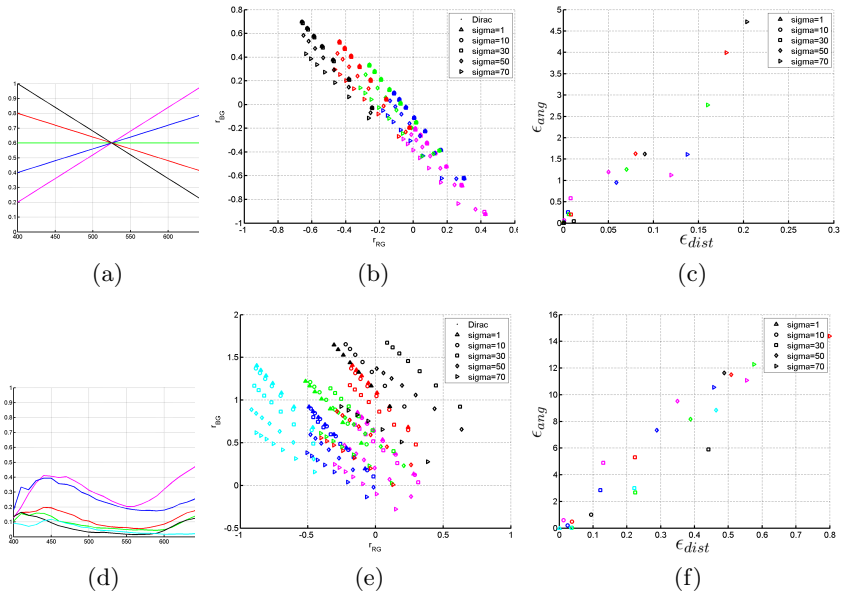

Fig. 4. Results of synthetic and natural albedo curves with changing narrowness of the sensor sensitivities. Left: Surface reflectances. Middle: LCS values; the values for $\sigma \in \{1, 10, 30\,nm\}$ almost fall on each other. Right: Error scatter plot.

4.5 Influence of Sensor Narrowness and Image Gamma

In order to analyze the influence of the narrowness on the errors, we also modeled sensor sensitivities as Gaussian curves with $\mu \in \{450, 530, 590\,nm\}$ and different widths, $\sigma \in \{1, 10, 30, 50, 70\,nm\}$. Examples for results on synthetic and natural reflectance curves are given in Fig.4. As expected decreasing bandwidth results in decreasing errors. This tendency could be observed in all the analyzed curves, independent of the shape of the surface spectra.

We also tested the effects of different gamma-values. A value of $\gamma > 1$ results in a compression of the LCS values. In almost 100% of the synthetic data and about 70% of the natural data $\gamma = 2.2$ resulted in an increased ϵ_{dist} and a reduced ϵ_{ang}. Sample plots are provided in the supplemental material.

4.6 Favorable Reflectance Spectra

Due to the observation that slightly increasing albedo curves (higher red and lower blue component) fit well to the NBA, we performed an additional evaluation on skin reflectance curves. Based on the melanin absorption, skin reflectance curves tend to have this advantageous shape (see Fig. 8(a)).

As expected, in LCS, the skin values cluster well (see Fig. 8(b)). Still, the performance of the more narrow SFU spectral sensitivities is better. This is also supported by the error scatter plot in Fig. 8(c). We want to emphasize

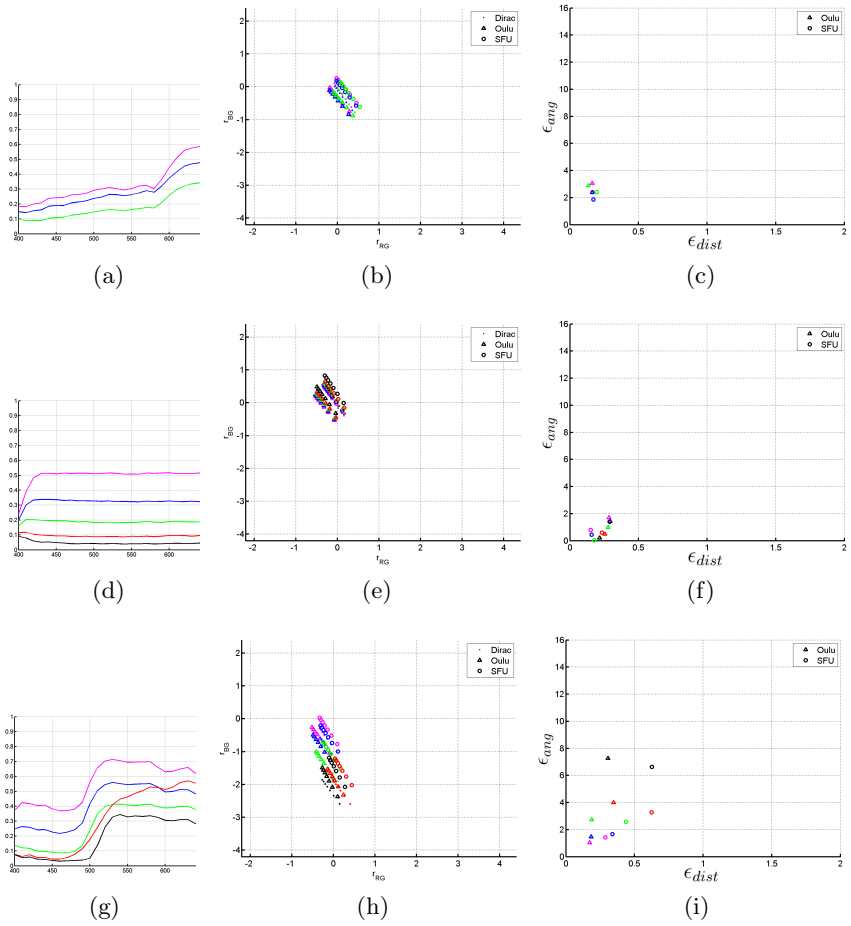

Fig. 5. Results for real reflectances (different shape categories). Left: Color-coded surface reflectances. Middle: LCS values. Right: Error scatter plot.

that reported errors are very good results compared to the average error of the arbitrary albedos of the CAVE database. Tab. 1 illustrates this, by showing the mean and standard deviation of the skin reflectance curves and the extracted spectra of the CAVE database.

Tab. 2 lists the best and worst measured errors for the CAVE database and Oulu sensor sensitivities. The corresponding spectra are shown in Fig. 3(b). The table reveals, how the performance is dependent on the sensor sensitivities (e.g. ϵ_{dist} for cyan). See supplemental material for further results.

	Oulu		SFU	
	ϵ_{dist}	ϵ_{ang}	ϵ_{dist}	ϵ_{ang}
CAVE	0.398 ± 0.273	$5.128^\circ \pm 3.913^\circ$	0.449 ± 0.310	$3.718^\circ \pm 2.864^\circ$
Skin	0.192 ± 0.020	$3.924^\circ \pm 0.848^\circ$	0.146 ± 0.012	$3.226^\circ \pm 0.716^\circ$

Table 1. Mean and standard deviation for the average distance ϵ_{dist} and the angular errorϵ_{ang} computed for the CAVE database and the skin reflectances. Both analyzed sensor sensitivities are listed separately.

	Oulu		SFU	
	ϵ_{dist}	ϵ_{ang}	ϵ_{dist}	ϵ_{ang}
CAVE min(ϵ_{dist}) for Oulu (cyan)	**0.07**	0.01°	0.44	1.00°
CAVE max(ϵ_{dist}) for Oulu (blue)	**1.71**	16.37°	0.93	12.86°
CAVE min(ϵ_{ang}) for Oulu (magenta)	0.21	$\mathbf{0.01}^\circ$	0.37	1.67°
CAVE max(ϵ_{ang}) for Oulu (green)	1.03;	$\mathbf{16.72}^\circ$	0.59	11.38°

Table 2. Spectra with the minimal and maximal errors of the CAVE database and Oulu sensor sensitivities. The corresponding curves (see color) are shown in Fig. 3(b).

5 Conclusions

This paper addressed the influence of the violation of the NBA on the results in LCS are addressed. The introduced error depends on the the color temperature of the illuminant, the sensor sensitivities and the surface reflectance. Due to the image formation process, these three factors are not separable. In our evaluation we, therefore, concentrated on the color of the captured materials. Our theoretical formulation of the NBA-deviation showed that: when the ratio of the errors in the blue and red channels approximates the ratio of the respective Dirac delta values, the violation of the NBA leads to insignificantly small errors. Our analysis was based on two error metrics. These were designed so as to evaluate the suitability of reflectances for two groups of applications: illumination invariance and clustering/segmentation in LCS. In our analysis on synthetic and real surface reflectances it turned out that especially for bright and unsaturated colors, like skin color, the error in LCS is very small. Object colors with large errors, will benefit from spectral sharpening. Furthermore, due to Eq.10, the band which is less balanced with respect to the other two bands should be selected as the normalizing channel in Eq.4.

6 Acknowledgments

The authors gratefully acknowledge funding of the Erlangen Graduate School in Advanced Optical Technologies (SAOT) by the German National Science Foundation (DFG) in the framework of the excellence initiative. Eva Eibenberger is supported by the International Max Planck Research School for Optics and Imaging.

References

1. Finlayson, G., Drew, M., Lu, C.: Intrinsic Images by Entropy Minimization. In: European Conference on Computer Vision. (2004) 582–595
2. Tan, R., Nishino, K., Ikeuchi, K.: Color Constancy through Inverse-Intensity Chromaticity Space. Journal of the Optical Society of America A **21** (2004) 321–334
3. Barnard, K., Finlayson, G.: Shadow Identification Using Colour Ratios. In: Color Imaging Conference. (2000) 97–101
4. Finlayson, G., Hordley, S., Lu, C., Drew, M.: On the Removal of Shadows from Images. IEEE Transactions on Pattern Analysis and Machine Intelligence **28** (2006) 59–68
5. Álvarez, J., López, A., Baldrich, R.: Illuminant-Invariant Model-Based Road Segmentation. In: IEEE Intelligent Vehicles Symposium. (2008) 1175–1180
6. Finlayson, G.D., Drew, M.S., Lu, C.: Entropy Minimization for Shadow Removal. International Journal of Computer Vision **85** (2009) 35–57
7. Tian, J., Sun, J., Tang, Y.: Tricolor Attenuation Model for Shadow Detection. IEEE Transactions on Image Processing **18** (2009) 2355–2363
8. Finlayson, G., Fredembach, C., Drew, M.: Detecting illumination in images. In: IEEE International Conference on Computer Vision. (2007)
9. Finlayson, G.D., Hordley, S.D.: Color Constancy at a Pixel. Journal of the Optical Society of America A **18** (2001) 253–264
10. Xu, L., Qi, F., Jiang, R., Hao, Y., Wu, G., Xu, L., Qi, F., Jiang, R., Hao, Y., Wu, G.: Shadow Detection and Removal in Real Images: A Survey. Technical report, Shanghai Jiao Tong University (2006)
11. Álvarez, J., López, A., Baldrich, R.: Shadow Resistant Road Segmentation from a Mobile Monocular System. In: Iberian Conference on Pattern Recognition and Image Analysis. (2007) 9–16
12. Zhang, G., Dong, Z., Jia, J., Wan, L., Wong, T., Bao, H.: Refilming with Depth-Inferred Videos. IEEE Transactions on Visualization and Computer Graphics **15** (2009) 828–840
13. Drew, M., Finlayson, G.: Spectral Sharpening with Positivity. Journal of the Optical Society of America A **17** (2000) 1361–1370
14. Barnard, K., Ciurea, F., Funt, B.: Sensor Sharpening for Computational Color Constancy. Journal of the optical society of america A **18** (2001) 2728–2743
15. Drew, M., Joze, H.: Sharpening from Shadows: Sensor Transforms for Removing Shadows using a Single Image. In: Color Imaging Conference. (2009) 267–271
16. Barnard, K., Funt, B., Burnaby, B.: Experiments in Sensor Sharpening for Color Constancy. In: Color Imaging Conference. (1998) 43–46
17. Kawakami, R., Takamatsu, J., Ikeuchi, K.: Color Constancy from Blackbody Illumination. Journal of the Optical Society of America A **24** (2007) 1886–1893
18. Henderon, S., Hodgkiss, D.: The Spectral Energy Distribution of Daylight. British Journal of Applied Physics **15** (1964) 947–952
19. Yasuma, F., Mitsunaga, T., Iso, D., Nayar, S.: Generalized Assorted Pixel Camera: Post-Capture Control of Resolution, Dynamic Range and Spectrum,. Technical Report CUCS-061-08, Department of Computer Science, Columbia University (2008)
20. Marszalec, E., Martinkauppi, B., Soriano, M., Pietikäinen, M.: Physics-based Face Database for Color Research. Journal of Electronic Imaging **9** (2000) 32–38
21. Barnard, K., Martin, L., Funt, B., Coath, A.: A Data Set for Colour Research. Color Research and Application **27** (2002) 147–151

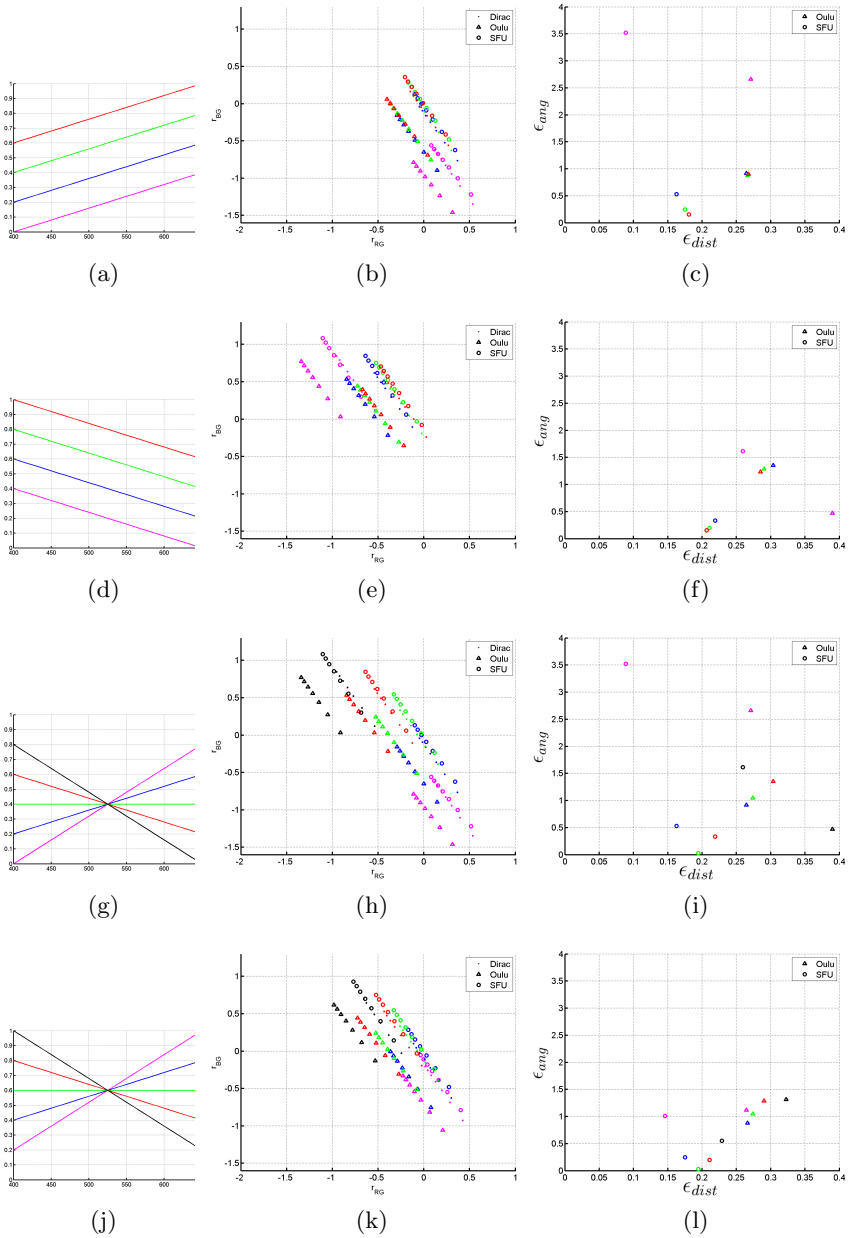

Fig. 6. Results for synthetic reflectances (different slopes and intensity levels). Left: surface reflectances. Middle: LCS values. Right: Error scatter plot.

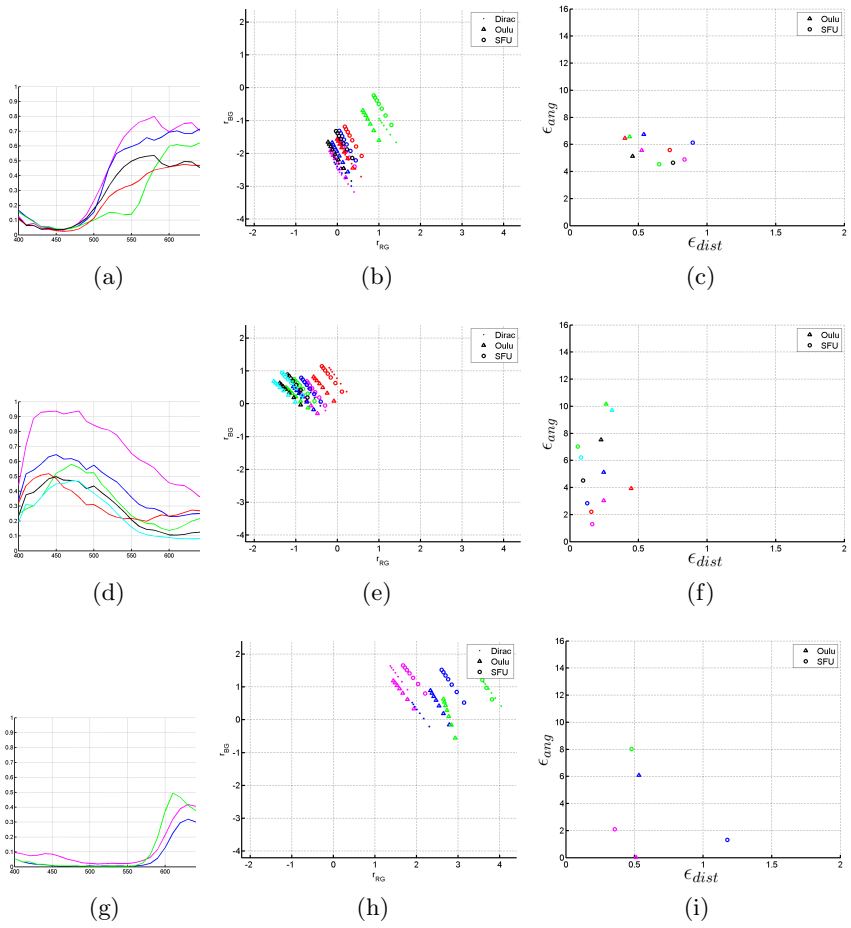

Fig. 7. Results for real reflectances (different shape categories). Left: Color-coded surface reflectances. Middle: LCS values. Right: Error scatter plot.

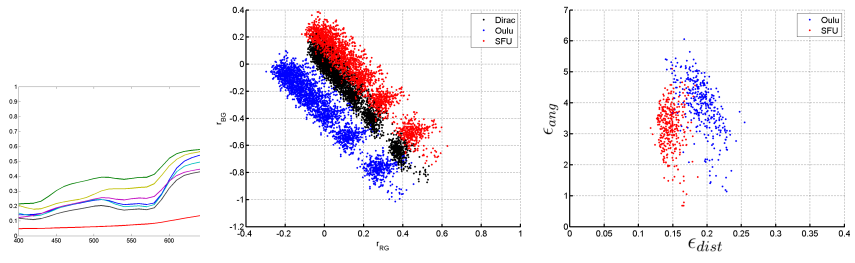

Fig. 8. Results of skin albedo curves. Left: Skin reflectances. Middle: LCS values. Right: Error scatter plot.